# Nonlinearity-enabled localization in driven-dissipative photonic lattices

A. Muñoz de las Heras [1,*] A. Amo [2] and A. González-Tudela [1]
[1]*Institute of Fundamental Physics, CSIC, Calle Serrano 113b, 28006 Madrid, Spain*
[2]*Physique des Lasers Atomes et Molécules, UMR No. 8523, CNRS, Université de Lille, 59000 Lille, France*

(Received 2 April 2024; accepted 12 June 2024; published 28 June 2024)

Recent experimental work has demonstrated the ability to achieve reconfigurable photon localization in lossy photonic lattices by continuously driving them with lasers strategically positioned at specific locations. This localization results from the perfect destructive interference of light emitted from different positions and, because of that, occurs only at very specific frequencies. Here we examine this localization regime in the presence of standard optical Kerr nonlinearities, such as those found in polaritonic lattices, and show that they stabilize driven-dissipative localization in frequencies different from those observed in the linear regime. Moreover, we demonstrate that, contrary to intuition, in most situations this driven-dissipative localization does not enhance nonlinear effects like optical bistabilities, due to a concurrent reduction in overall intensities. Nevertheless, we are able to identify certain parameter regions where nonlinear enhancement is achieved, corresponding to situations where emission from different spots constructively interferes.

DOI: 10.1103/PhysRevA.109.063523

## I. INTRODUCTION

Localization of waves is a ubiquitous interference phenomenon present in various fields, including solid-state physics [1,2], acoustics [3,4], and photonics [5–7]. In the photonic context, beyond its fundamental interest, localization can be exploited to increase light-matter coupling strengths, with applications in quantum information [8], quantum communication [9–11], and quantum simulation [12,13]. To achieve such photon localization, several strategies have been explored, including the use of highly reflective mirrors in vacuum [8], exploiting the confinement of light in materials with high refractive indices [14,15], employing photonic crystals with a nontrivial topology leading to localized modes at their boundaries [16,17], and, perhaps the most exotic, engineering bound states in the continuum. The latter appear when the localized waves coexist with a continuum spectrum of propagating modes protected by symmetry or separability [18,19], and they have recently been predicted to arise also in the many-body regime [20,21]. In all these cases, however, the spatial nature of the localization is fixed by design and cannot be easily altered once the structure is built, limiting its versatility.

A recent experimental work [22] has demonstrated a new way forward to achieve reconfigurable photon localization in lossy photonic lattices by exploiting the interplay of continuous local drivings and nontrivial energy dispersions. The idea consists in placing several coherent pumps in judiciously chosen positions so that the light emitted from them destructively interferes and localizes within the region between them, being able to obtain highly nontrivial spatial patterns through appropriate laser modulation [23]. As so far considered, the method presents two limitations: First, it only works for specific laser frequencies where the perfect destructive interference takes place; second, it was designed and tested in the linear regime [22,23], so that whether it works in the presence of nonlinearities is still an open question.

In this work we address both limitations by investigating driven-dissipative localization in photonic lattices with Kerr nonlinearities [13,24]. Our analysis reveals two counterintuitive conclusions. First, nonlinearities do not hinder driven-dissipative localization despite the nonhomogeneous spatial distribution of the localization; in fact, they enable its existence at different frequencies from those observed in purely linear lattices. Second, in spite of such localization, nonlinear effects, like optical bistabilities, are weaker than in nonlocalized situations due to the smaller overall intensity in the former case. On the contrary, our study suggests that it is the opposite driving regime, in which the emission between the coherent pumps interferes constructively, that leads to an enhancement of nonlinear optical effects.

The paper is organized as follows. In Sec. II we introduce the driven-dissipative setups considered throughout this paper, along with the theoretical tools used to model them. Sections III and IV focus on a one-dimensional lattice with first-neighbor couplings. In Sec. III we characterize the phenomenon of driven-dissipative localization in the linear regime, providing analytical expressions for the local and total intensities. In Sec. IV we analyze the nonlinear regime, concentrating on the stability of the localization and the potential enhancement or diminishment of optical bistability. In Sec. V we demonstrate the generality of our results by considering a two-dimensional square lattice. We summarize our conclusions and provide an outlook for future work in Sec. VI.

## II. DRIVEN-DISSIPATIVE PHOTONIC LATTICES

Here we study the driven-dissipative steady states of one-dimensional (1D) and 2D photonic lattices formed by coupled

*Contact author: alberto.munoz@iff.csic.es

 

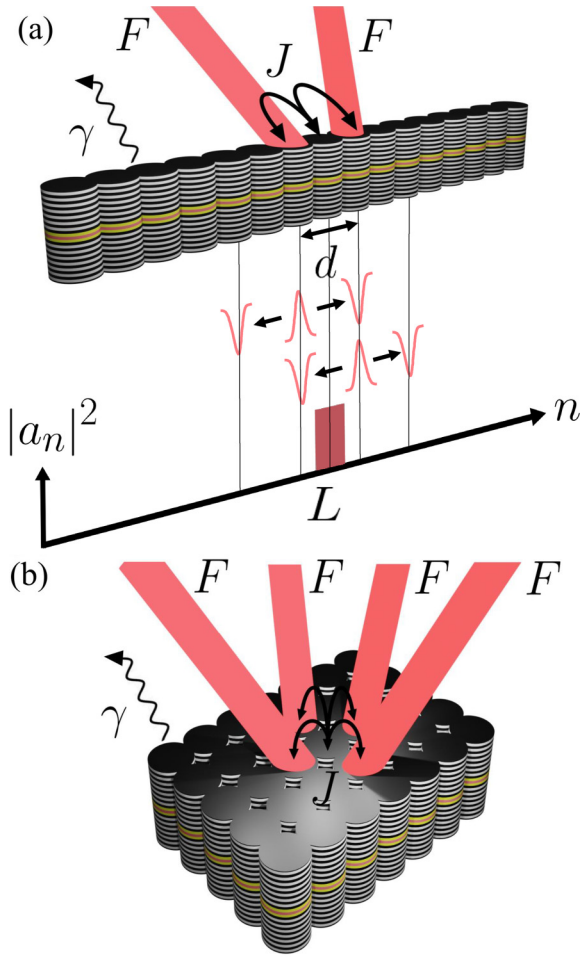


FIG. 1. (a) Scheme of a one-dimensional lattice of semiconductor micropillars hosting exciton polaritons, featuring first-neighbor couplings $J$ and photon cavity decay rate $\gamma$, and driven by two coherent pumps with the same amplitude $F$. Localization takes place between two sites separated a distance $d$ when there is destructive interference between the coherent light injected at the pumped sites. For instance, when $d = 2$ this results in a single site labeled $n = L$ concentrating all the intensity in the lattice $|a_L|^2$. (b) Analogous scheme for a two-dimensional square lattice. In this case, lasers of equal amplitude $F$ pump four sites of the lattice encircling a single site in which localization takes place.

optical cavities with Kerr nonlinearities. Our mathematical description is quite general and does not assume any specific implementation. However, a key aspect of our work is that it applies to driven-dissipative photonic resonators. As examples of physical systems where our ideas could be realized, we can mention arrays of semiconductor micropillars hosting exciton polaritons [13,17,25,26] [like the ones depicted in Figs. 1(a) and 1(b) for the 1D and 2D cases, respectively] and lattices of coupled superconducting cavities in the microwave regime [27–30]. More information about the experimental implementation of our ideas can be found in Appendix A. In general, the temporal dynamics and stationary states of these systems are described by the set of coupled-mode equations governing the amplitude of the electric field at each site $a_n$ [31,32],

$$i\dot{a}_n = \omega_a a_n - i\gamma a_n + U|a_n|^2 a_n - \sum_{\langle m\neq n\rangle} J_{n,m} a_m + F_n e^{-i\omega_P t}, \tag{1}$$

where the latin letters $n$ and $m$ indicate the lattice site indices running $1,\ldots,N$ and $1,\ldots,N^2$ in the 1D and 2D cases, respectively, with $N$ the system size in one dimension (throughout the paper we consider lattices with open boundary conditions); each site of the lattice corresponds to a single-mode resonator of bare resonance frequency $\omega_a$ and decay rate $\gamma$, which we assume to be equal for every site; $J_{n,m}$ is the tunneling rate between sites $m$ and $n$ (taken as a real number, since in this work we are not dealing with gauge fields [16]), which we restrict here to first-neighbor terms (in which $J_{\langle n,m\rangle} \equiv J$); $F_n$ is the coherent pump amplitude at site $n$ that oscillates in time $t$ with a frequency $\omega_P$, which we consider to be the same for all $n$; and finally $U$ is a Kerr-type nonlinear frequency shift that can appear, e.g., in polaritonic lattices due their matter component [13] and that we also assume to be equal at all sites.

To find the steady states of Eq. (1) we use a fourth-order Runge-Kutta routine to solve the dynamics and run it until converged results are obtained. Codes to reproduce the figures of the paper are available in [33].

## III. LOCALIZATION IN A ONE-DIMENSIONAL PHOTONIC LATTICE WITHIN THE LINEAR REGIME

Let us start by reviewing and extending the results obtained in Refs. [22,23] in the linear regime for one-dimensional photonic lattices [i.e., taking $U = 0$ in Eq. (1)]. To analyze the emergence of driven-dissipative localization in such scenario, it is convenient to choose a rotating frame with the laser frequency $\omega_P$. Therefore, one can write the field amplitudes in Eq. (1) as $a_n \to a_n e^{-i\omega_P t}$. Then it is also convenient to assume periodic boundary conditions to expand $a_n$ in its Fourier components, i.e., $a_n = (1/\sqrt{N})\sum_k a_k e^{-ikn}$, with $k$ the associated momenta. Putting together these two considerations, Eq. (1) can be written as

$$i\dot{a}_k = [\omega(k) - \omega_P]a_k - i\gamma a_k + F_k, \tag{2}$$

with $F_k = (1/\sqrt{N})\sum_n F_n e^{-ikn}$ the $k$ dependence of the coherent pump and $\omega(k)$ the energy dispersion of the photonic lattice which reads

$$\omega(k) = \omega_a - 2J\cos(k). \tag{3}$$

The steady-state solution of Eq. (2) can be found by setting $\dot{a}_k = 0$, obtaining

$$a_k(t\to\infty) = \frac{F_k}{\omega_P - \omega(k) + i\gamma}. \tag{4}$$

In the equation above, we can see that the most populated modes in momentum space will be those satisfying

$$\omega(k_a) = \omega_P \to k_a = \pm\arccos\left(\frac{-\Delta}{2J}\right), \tag{5}$$

where $\Delta = \omega_P - \omega_a$ is the pump-resonator detuning. The predominance of such values of momentum makes it possible

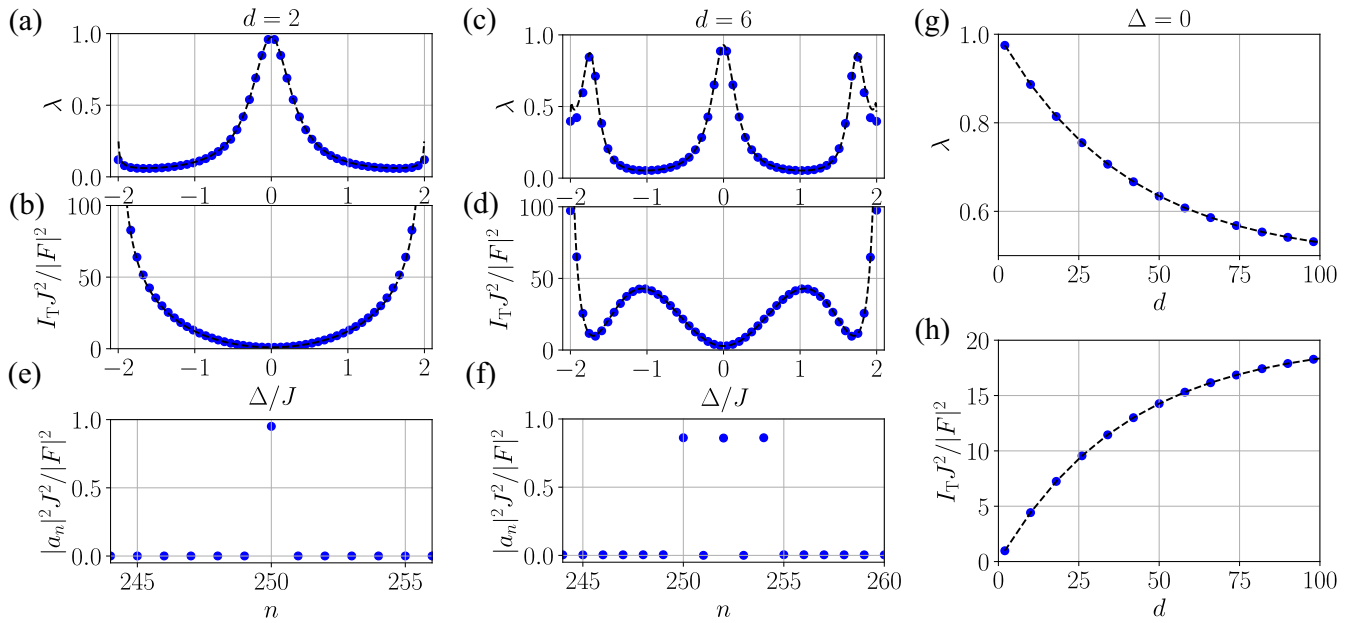


FIG. 2. Analysis of localization in a linear ($U = 0$) one-dimensional photonic lattice with first-neighbor couplings featuring two local pumps with equal amplitude. (a) and (c) Localization $\lambda$ and (b) and (d) total intensity in the lattice $I_T$ (in units of the tunneling $J$ and the pump intensity $|F|^2$) as a function of the detuning $\Delta$ for interpump distances (a) and (b) $d = 2$ and (c) and (d) $d = 6$. The intensity $|a_n|^2$ at each site $n$ of the lattice is plotted for $\Delta = 0$ and (e) $d = 2$ and (f) $d = 6$. (g) Localization $\lambda$ and (h) total intensity $I_T$ for a fixed $\Delta = 0$ and as a function of $d$. In all panels, blue circles are the results of numerical simulations to find the steady state of Eq. (1), while dashed lines correspond to the analytical results obtained with Eqs. (9) and (10). The parameters are the cavity decay rate $\gamma = 5 \times 10^{-2} J$, $N = 500$ sites with open boundary conditions, and $n_1 = 250$.

that, when several pumps drive the photonic lattice at different sites, they can interfere constructively or destructively depending on their relative position. For instance, if one drives the lattice at two positions $n_{1,2}$, the emission from each spot will acquire a phase $e^{ik_a d}$ after traveling through the interpump distance $d = n_1 - n_2$. Thus, if the drivings are equal in amplitude and phase, when the distance $d$ and momentum $k_a$ are such that

$$1 + e^{ik_a d} = 0, \tag{6}$$

destructive interference occurs at all sites to the left and to the right of both spots and therefore the emission remains fully localized in between the two drivings. This mechanism is schematically depicted in Fig. 1(a). For instance, at a detuning $\Delta = 0$ where the resonant pump momenta given by Eq. (5) are $k_a = \pm\pi/2$, localization occurs at distances $d = 2(2\ell + 1)$, where $\ell \in \mathbb{Z}$. As shown in Refs. [22,23], localization can be perfect in the limit of small losses, i.e., when $\gamma \to 0$. However, even in that case, dephasing effects can destroy the coherence of the light emitted by each site, thus precluding perfect localization [34].

In Fig. 2 we illustrate this localization for two different distances between the pumping spots, $d = 2$ and 6, in the left and middle columns, respectively. To quantify localization, we define the parameter

$$\lambda = \frac{\sum_{n_1<n<n_2} |a_n|^2}{I_T}, \tag{7}$$

which accounts for the fraction of intensity in the region between the pumps with respect to the total intensity inside the lattice $I_T = \sum_n |a_n|^2$. In Figs. 2(a) and 2(c) we plot as blue circles the localization parameter $\lambda$ and the total intensity [Figs. 2(b) and 2(d)] as a function of the detuning $\Delta$ for $d = 2, 6$, obtained by solving numerically the coupled-mode equations (2). There one can observe that for $d = 2$ [Fig. 2(a)] $\lambda$ has a single maximum (at $\Delta = 0$), whereas for $d = 6$ [Fig. 2(c)] several maxima appear. This can be understood by substituting the value of the resonant momentum $k_a$ given by Eq. (5) into the localization condition in Eq. (6). This implies that the values of detuning at which localization maxima appear are given by

$$\Delta_\ell = -2J \cos\left(\frac{(2\ell + 1)\pi}{d}\right), \tag{8}$$

where $\ell \in \mathbb{Z}$. For $d = 2$ the equation above only allows a localization maximum at $\Delta = 0$. However, for $d = 6$ there are three integers ($\ell = 0, 1, 2$) leading to localization maxima at three different values $\Delta \simeq -1.73J$, 0, and $1.73J$.

For both $d = 2$ and 6, when one takes a value of $\Delta$ leading to a localization maximum, the steady-state spatial population is localized between the pumping spots. As an example, Figs. 2(e) and 2(f) show the intensity distribution in real space $|a_n|^2$ with interpump distances $d = 2, 6$, respectively, both for a fixed detuning $\Delta = 0$ in which $\lambda$ features a maximum for both distances. Interestingly, these localization maxima appear in frequency regions where the total intensity $I_T$ is minimum, as shown in Figs. 2(b) and 2(d). This minimum was inadvertently passed in previous works and will have important consequences in the appearance of nonlinear effects, as we will see in Sec. IV. We note that, although close to zero, $I_T$ features a finite value at $\Delta = 0$ in Figs. 2(b) and 2(d).

To gain insight into the interplay between localization and total intensity, we obtain approximate analytical expressions for both the spatial profiles of the populations, $|a_n|^2$, as well as the total intensity $I_T$, which read (see Appendix B for details)

$$|a_n|^2 = \begin{cases} 2\pi^2|F|^2D(\Delta)^2 e^{-\pi\gamma D(\Delta)(n_1+n_2-2n)}\{\cosh[\pi\gamma D(\Delta)d] + \cos(k_0 d)\} & \text{if } n \leqslant n_1 \\ 2\pi^2|F|^2D(\Delta)^2 e^{-\pi\gamma D(\Delta)d}\{\cosh[\pi\gamma D(\Delta)(n_1+n_2-2n)] + \cos[k_0(n_1+n_2-2n)]\} & \text{if } n_1 \leqslant n \leqslant n_2 \\ 2\pi^2|F|^2D(\Delta)^2 e^{\pi\gamma D(\Delta)(n_1+n_2-2n)}\{\cosh[\pi\gamma D(\Delta)d] + \cos(k_0 d)\} & \text{if } n \geqslant n_2 \end{cases} \tag{9}$$

and

$$I_T = \frac{2\pi|F|^2D(\Delta)}{\gamma}\left[1 + \cos(k_0 d)e^{-\pi\gamma D(\Delta)d}\right], \tag{10}$$

respectively, where $D(\Delta)$ is the density of states of the one-dimensional photonic lattice:

$$D(\Delta) = \frac{1}{N}\sum_k \delta(\Delta + 2J\cos k) = \frac{1}{\pi}\frac{1}{\sqrt{4J^2 - \Delta^2}}. \tag{11}$$

These expressions provide a very clear picture of the dependence of the results on some relevant photonic lattice figures of merit, like the density of states or photon-decay rate. Plotted as dashed lines in Figs. 2(a)–2(d), we see that they feature perfect agreement with the numerical results. The only significant deviations appear near the band edges, $\Delta = \pm 2J$, where the approximations used to derive Eqs. (9) and (10) are not valid (see Appendix B for details).

From the analytical expression of the total intensity [Eq. (10)], we can obtain two conclusions. First, we can immediately see that the localization condition of Eq. (6) implies at the same time a diminished total intensity. In Appendix C we explain that in terms of the analogy put forward in Ref. [23] and show that $I_T$ is just proportional to the local density of states [35–37] of two emitters coupled to the bath at sites $n_1$ and $n_2$. Thus, this decrease of the total intensity can be understood as an inefficient coupling of the ensemble of the two pumping spots to the photonic lattice. Second, the total intensity is maximized due to two effects: by the increase of the density of states $D(\Delta)$ in slow light regions, i.e., at the band edges of our 1D lattice, where the group velocity $v_g = \partial\omega/\partial k = [\pi D(\Delta)]^{-1}$ vanishes [38,39], and, complementarily, at the regions corresponding to constructive interference, i.e., $1 - e^{ik_a d} = 0$ for this choice of pumping spot phases, where there is a collective enhancement of the intensity.

This condition of constructive interference allows us to calculate an expression similar to Eq. (8), but in this case accounting for the values of detuning where $I_T$ features a maximum,

$$\Delta_\ell = -2J\cos\left(\frac{2\ell\pi}{d}\right), \tag{12}$$

where $\ell \in \mathbb{Z}$. This is in agreement with the results of our numerical simulations shown in Figs. 2(b) and 2(d), where maxima of $I_T$ can be found at $\Delta = -2J$ and $2J$ for $d = 2$ and at $\Delta = -2J, -J, J$, and $2J$ for $d = 6$. These values of $\Delta$ also correspond to minima of $\lambda$.

Finally, apart from explaining such an interplay between localization and total intensity, Eqs. (9) and (10) allow understanding the dependence of both $\lambda$ and $I_T$ for different interpump distances $d$. Since both $d$ and $\gamma$ appear in the exponential function of Eq. (10), we expect that increasing one of such quantities will spoil perfect localization and conversely produce an increase in $I_T$. This is indeed observed in Figs. 2(g) and 2(h): For a fixed detuning $\Delta = 0$ the localization (total intensity) decreases (increases) for growing $d$. Such results are confirmed by the numerical simulations shown as blue circles.

## IV. NONLINEAR DRIVEN-DISSIPATIVE LOCALIZATION EFFECTS: STABILITY AND ENHANCEMENT

In this section we study how the driven-dissipative localization scenario changes when one includes sizable Kerr nonlinearities, i.e., $U \neq 0$. Without loss of generality, we restrict our study to positive values of $U$. As can be seen in Eq. (1), we consider local nonlinearities that modify the on-site energy of each site by a factor $U|a_n|^2$. *A priori*, since the steady-state population profiles $|a_n|^2$ are not uniform [see Figs. 2(e) and 2(f)], it is unclear whether localization survives in the nonlinear regime and if it does whether it enhances nonlinear phenomena such as optical bistabilities. We answer these two questions in Secs. IV A and IV B, respectively.

### A. Stability of driven-dissipative localization

Let us start by analyzing the behavior of the localization parameter $\lambda$ and the total intensity $I_T$ for a growing nonlinearity. For that we produce contour plots of $\lambda$ and $I_T$ as a function of the adimensional quantities $\Delta/J$ and $U|F|^2/J^3$ in Figs. 3(a) and 3(c) and Figs. 3(b) and 3(d), respectively. Figures 3(a) and 3(b) are calculated for an interpump distance $d = 2$, while Figs. 3(c) and 3(d) correspond to $d = 6$.

Focusing first on the localization parameter, we observe that, contrary to intuition, localization survives for nonzero values of $U$ in frequency regions forbidden in the linear regime. Let us consider, for example, the case of $d = 2$, where localization in the linear regime occurs only at $\Delta = 0$. In the nonlinear regime, however, the value of $\Delta$ leading to the maximum localization follows the relation $\Delta = U|F|^2/J^2$ [indicated by the red dashed line in Figs. 3(a) and 3(b)] up to a point where it suddenly decreases due to dynamical instabilities induced by the parametric couplings introduced by the Kerr nonlinearity [13,40–43] (more information about this phenomenon can be found in Appendix D). Nevertheless, the driven-dissipative localization remains very high, i.e., $\lambda \geqslant 0.9$, for values of detuning approximately in the region $\Delta \in (0, 0.5J)$, something that would be impossible within the linear regime. We refer to this phenomenon as nonlinearity-enabled localization.

In Figs. 3(c) and 3(d) a similar analysis is carried for an interpump distance $d = 6$. In agreement with the results of Sec. III, we observe that in the linear regime, i.e., for $U = 0$,

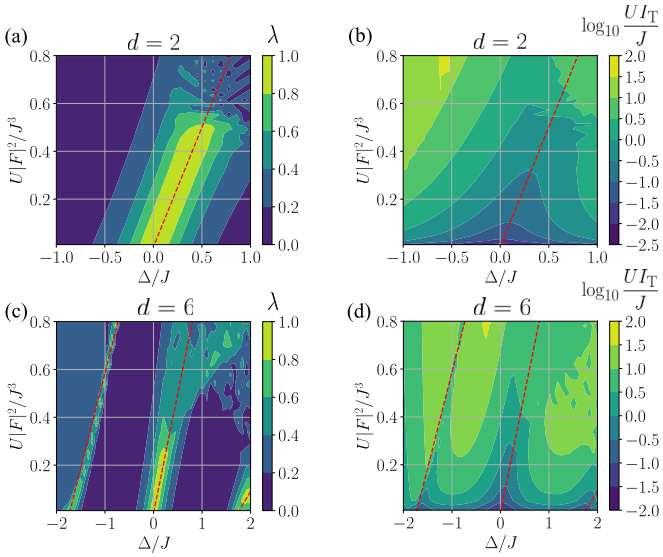


FIG. 3. Localization in the nonlinear 1D lattice. The localization parameter $\lambda$ is plotted for interpump distances (a) $d = 2$ and (c) $d = 6$ as a function of the pump amplitude $|F|^2$ (normalized in units of the Kerr nonlinearity strength $U$ and the tunneling rate $J$) and the detuning $\Delta$. The analogous plot for the total intensity inside the lattice $I_T$ is calculated for (b) $d = 2$ and (d) $d = 6$. In all panels, red dashed lines signal the dependence $\Delta = \Delta_\ell + \alpha_\ell U|F|^2/J^2$ of the detuning at which localization maxima (and $I_T$ minima) appear (see the text). The simulation parameters are the cavity decay rate $\gamma = 5 \times 10^{-2}J$, $N = 500$ sites with open boundary conditions, and $n_1 = 250$.

the localization features maxima for three detunings given by Eq. (8), which are shifted towards higher values of $\Delta$ when $U \neq 0$, following the relation $\Delta = \Delta_\ell + \alpha_\ell U|F|^2/J^2$, with $\alpha_\ell$ a constant that depends on $\ell$. While for the central localization region given by $\Delta_1$ we can take $\alpha_1 = 1$ (thus recovering the dependence of the $d = 2$ case), $\alpha_\ell$ is larger than 1 for the other two localization regions appearing for $\Delta_0$ (which is fitted by $\alpha_0 \simeq 1.2$) and $\Delta_2$ (for which we estimate $\alpha_2 \simeq 2.8$). This is evident from Fig. 3(c), where we plot $\Delta = \Delta_\ell + \alpha_\ell U|F|^2/J^2$ as red dashed lines for $\ell = 0, 1, 2$. Furthermore, another difference with respect to $d = 2$ is that the dynamical instabilities appear for smaller values of $\Delta$ than in the $d = 2$ case.

We now focus on the behavior of the total intensity. In both cases $d = 2$ and 6, the nonlinear regime inherits the inverse relation between the localization parameter $\lambda$ and the total intensity $I_T$ found in Sec. III for the linear case. This is evidenced by Figs. 3(b) and 3(d), which display analogous contour plots of the total intensity $I_T$ as a function of $\Delta/J$ and $U|F|^2/J^3$ for $d = 2$ [Fig. 3(b)] and $d = 6$ [Fig. 3(d)]. Comparing these results with those of Figs. 3(a) and 3(c) for the localization parameter, we see that, also in the nonlinear regime, a large value of $\lambda$ is accompanied by a small $I_T$. To further clarify this point, the red dashed lines indicating the regions of maximum $\lambda$ in Figs. 3(a) and 3(c) are also plotted in Figs. 3(b) and 3(d) and demonstrate that these regions correspond to minima of $I_T$.

Finally, to analyze in more detail the limits of the nonlinear enabled localization, in Fig. 4 we plot the maximum

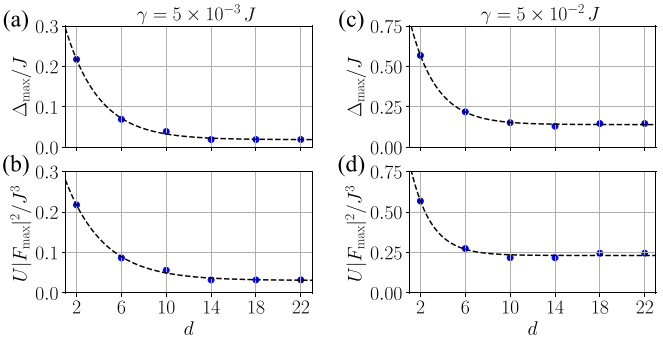


FIG. 4. Maximum values of (a) detuning $\Delta_{max}$ (normalized in units of the tunneling rate $J$) and (b) pump intensity $|F_{max}|^2$ (normalized in units of the Kerr nonlinearity strength $U$ and $J$) as a function of the interpump distance $d$, for the central localization region with detuning $\Delta = 0$ at $F = 0$. The cavity decay rate is fixed at $\gamma = 5 \times 10^{-3}J$. Blue dots are numerical results, while dashed lines correspond to exponential fits (see the text for details). (c) and (d) Analogous plots for $\gamma = 5 \times 10^{-2}J$. The simulation parameters are $N = 500$ sites with open boundary conditions and $n_1 = 250$.

values of $\Delta$ and $|F|^2$ in which localization drops below $\lambda = 0.9$ as a function of $d$, considering always the central localization region that appears at $\Delta = 0$ when $U = 0$. We label such maximum values as $\Delta_{max}$ and $|F_{max}|^2$, respectively. Figures 4(a) and 4(b) are calculated for a cavity decay rate $\gamma = 5 \times 10^{-3}J$, while Figs. 4(c) and 4(d) show analogous plots for $\gamma = 5 \times 10^{-2}J$. For the two values of $\gamma$, we observe that both $\Delta_{max}$ and $|F_{max}|^2$ follow an exponential decay and then saturate, reaching constant values that are independent of $d$. This is indicated by the dashed lines, which correspond to a fit to an exponential law, $f(x) = ae^{-bx} + c$, where $a$, $b$, and $c$ are the fit parameters. However, this saturation occurs for a smaller value of $d$ (around $d \simeq 10$) for $\gamma = 5 \times 10^{-2}J$, while for $\gamma = 5 \times 10^{-3}J$ it takes place around $d \simeq 14$. Moreover, for the same $d$, the values of $\Delta_{max}$ and $|F_{max}|^2$ are larger in the former case. This can be related to the role played by the cavity decay rate in stabilizing the steady-state solution of the coupled-mode equations (1).

### B. Enhancement of optical bistabilities

In principle, one would expect that driven-dissipative localization enhances nonlinear effects due to the concentration of light into a small number of sites [see Figs. 2(e) and 2(f)]. However, the trade-off between localization and total intensity in the linear and nonlinear regimes that we demonstrated in the preceding section points to the opposite direction. In this section we study the emergence of optical bistable behavior as a signature of optical nonlinear effects and demonstrate that, actually, the appearance of bistabilities is linked to the enhancement of the total intensity due to slow light and constructive interference rather than localization regions.

To show that, in Figs. 5(a)–5(c) we plot the bistability curves of the total intensity $I_T$ for two pumps separated by a distance $d = 6$ and increasing values of the adimensional parameter $U|F|^2/J^3$ quantifying the Kerr nonlinearity strength. The cyan circles (blue squares) represent the intensity for a rightward (leftward) ramp, i.e., for $\Delta$ going from negative

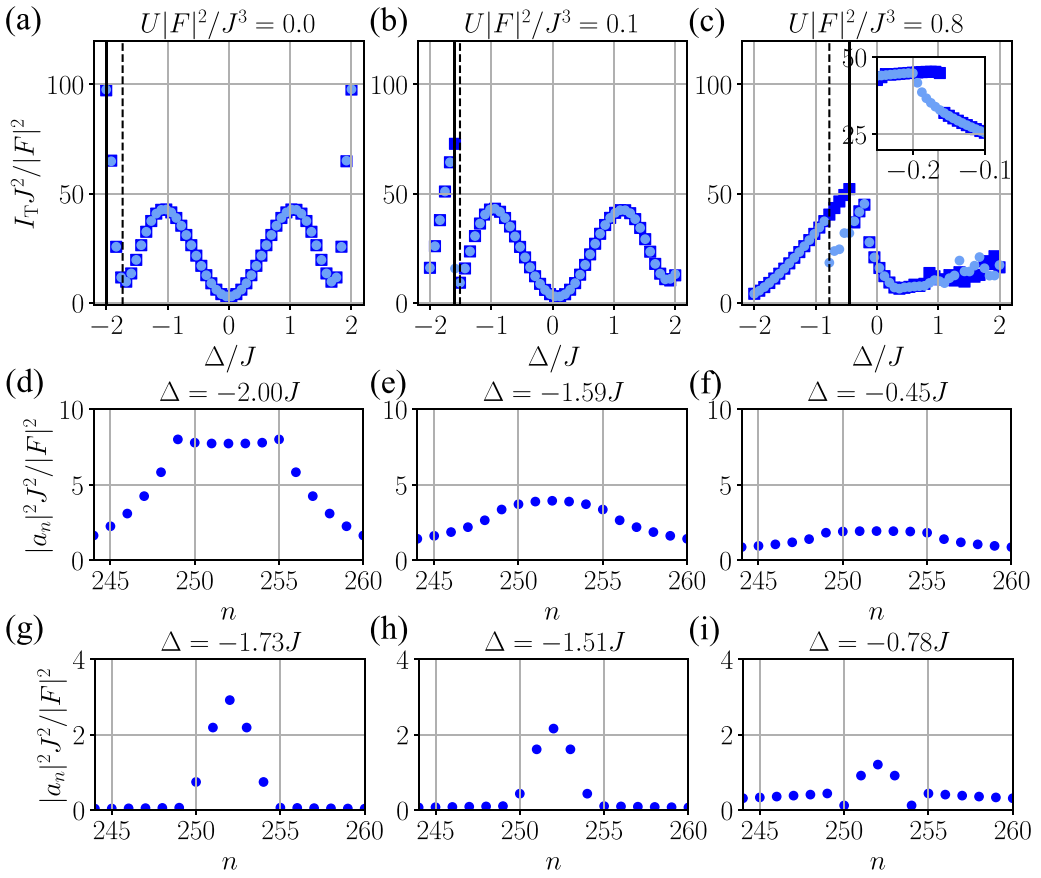


FIG. 5. (a)–(c) Total intensity inside the lattice $I_T$ normalized in units of the tunneling rate $J$ and the pump intensity $|F|^2$ as a function of the detuning $\Delta$, for an interpump distance $d = 6$. Each panel corresponds to a different value of the Kerr nonlinearity strength $U$. To make optical bistabilities visible, squares are the results of a rightward ramp (in which $\Delta$ is increased starting from the lower band edge), while circles belong to a leftward ramp (in which $\Delta$ is decreased starting from the upper band edge). The intensity $|a_n|^2$ at each site $n$ of the lattice is plotted for values of $\Delta$ in which $I_T$ reaches the (d)–(f) maximum and (g)–(i) minimum indicated by the vertical (d)–(f) solid and (g)–(i) dashed lines in (a)–(c), calculated for (d) and (g) $U|F|^2/J^3 = 0$, (e) and (h) $U|F|^2/J^3 = 0.1$, and (f) and (i) $U|F|^2/J^3 = 0.8$. The simulation parameters are the cavity decay rate $\gamma = 5 \times 10^{-2} J$, $N = 500$ sites with open boundary conditions, and $n_1 = 250$.

(positive) to positive (negative) values. In Fig. 5(a) we plot the situation with $U = 0$, i.e., the linear regime. In this case, there are obviously no bistabilities and thus squares and circles coincide. In Figs. 5(d) and 5(e) we plot the spatial patterns at $\Delta = -2J$ and $-1.73J$, corresponding to the first maximum and minimum of $I_T$ in Fig. 5(a) (starting from the bottom band edge) and indicated with black solid and dashed lines, respectively. There we see that the minimum (maximum) intensity corresponds to the situation with (without) localization.

We now study the displacement of such a maximum and minimum of $I_T$ for growing $U|F|^2/J^3$. In Fig. 5(b) we plot the total intensity for a small value of $U|F|^2/J^3 = 0.1$. In this case, the Kerr nonlinearity blueshifts the maxima and minima of $I_T$ towards larger values of detuning. In particular, the slow light enhancement of $I_T$, which takes place at $\Delta = -2J$ in the linear case, now generates a single bistability curve around $\Delta \simeq -1.59J$. It makes sense that such a maximum is the first one developing an optical bistability for growing $U|F|^2/J^3$, as it is the one reaching the largest $I_T$. On the other hand, the first minimum of $I_T$, located at $\Delta = -1.73J$ for $U = 0$, is now displaced to $\Delta = -1.51J$. In Figs. 5(e) and 5(h) we plot the spatial patterns corresponding to such a maximum (minimum) indicated by the solid (dashed) line in Fig. 5(b), showing that when $I_T$ reaches its maximum light spreads over all lattice sites, while when $I_T$ is minimum light is localized in the region between the pumps.

This behavior continues up to a critical value of $U|F|^2/J^3$ at which a second hysteresis cycle opens at the second intensity maximum (located at $\Delta = -J$ in the linear regime and blueshifted for a finite $U|F|^2/J^3$). Figure 5(c) shows the total intensity for $U|F|^2/J^3 = 0.8$, for which both optical bistabilities can be observed (the second one is displayed in the inset). At $\Delta \gtrsim 0$ a dynamical instability arises, in agreement with Fig. 3(b). Such a large value of $U|F|^2/J^3$ further blueshifts the first maximum (minimum) of $I_T$, which now takes place at $\Delta = -0.45J$ ($\Delta = -0.78J$) and is indicated by the solid (dashed) line. The spatial distribution of the intensity for these values of $\Delta$ is plotted in Figs. 5(f) and 5(i). The results of these figures confirm that a high intensity inside the lattice corresponds to light spreading over several resonators, while localization is found at values of detuning in which $I_T$ is minimum. Actually, in Fig. 5(i) localization is not perfect, as intensity leaks outside of the region between the pumps. This can be related to the fact that for $U|F|^2/J^3 = 0.8$ there is a larger value of $I_T$ at $\Delta = -0.78J$ in the lower bistability branch [see Fig. 5(c)] compared, for instance, with the smaller

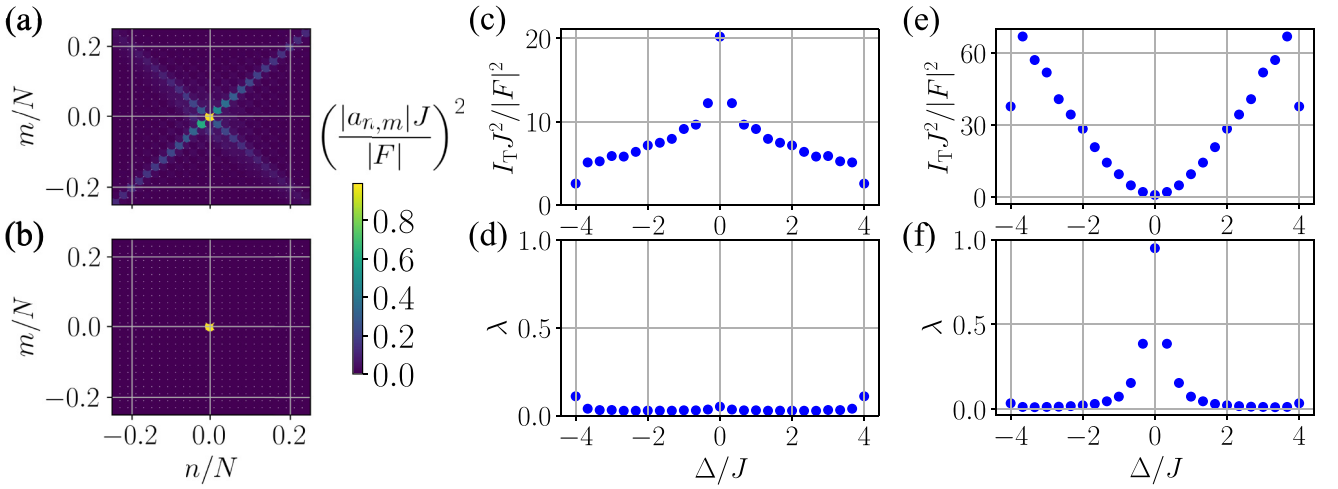


FIG. 6. Localization in the linear ($U = 0$) square lattice. (a) Spatial distribution of the intensity $|a_{n,m}|^2$ (normalized using the tunneling rate $J$ and the pump intensity $|F|^2$) for an $N \times N$ lattice coherently driven at its central site (0,0), i.e., individual driving. The detuning is fixed at $\Delta = 0$. (b) Analogous plot for a lattice driven by four pumps located at $(\pm 1, 0)$ and $(0, \pm 1)$, i.e., collective driving, where the intersite distance is 1. (c) Total intensity in the lattice $I_T$ in the individual driving configuration as a function of the detuning $\Delta$. (d) Analogous plot for the localization parameter $\lambda$. (e) Total intensity in the lattice $I_T$ in the collective driving configuration as a function of the detuning $\Delta$. (f) Analogous plot for the localization parameter $\lambda$. The simulation parameters are the cavity decay rate $\gamma = 5 \times 10^{-2} J$ and $N = 50$, i.e., $50 \times 50$ sites, with open boundary conditions.

value of $I_T$ that appears for $U|F|^2/J^3 = 0.1$ at $\Delta = -1.51J$ [see Fig. 5(b)]. This implies a better localization in the latter case, with almost no intensity outside the region between the pumps [see Fig. 5(h)].

Overall, the results of this section demonstrate that localization is not linked to an enhancement of nonlinear effects. Actually, it takes place at values of detuning for which the total intensity $I_T$ features a local minimum. On the contrary, nonlinear phenomena such as optical bistabilities appear when the intensity inside the lattice is maximum. Such a situation is associated with either slow light effects or a constructive interference between the two pumps, implying a spreading of light over the whole lattice.

## V. EXTENSION TO TWO-DIMENSIONAL LATTICES

In this section we show that the previous conclusions of the nonlinear driven-dissipative localization can also be extended to 2D lattices. In particular, we consider a square lattice formed by $N \times N$ sites with first-neighbor couplings [depicted in Fig. 1(b)]. We start by addressing the linear regime. This was extensively studied in Refs. [22,23], where it was shown that the driven-dissipative localization can also occur in 2D geometries. However, this is again limited to specific frequencies, as it was for 1D lattices.

As a first step, we reproduce the behavior of linear square lattices observed in Ref. [23] as well as check that the inverse relation between localization and total intensity revealed in the 1D case also holds in two dimensions. By setting $U = 0$, the coupled-mode equations (1) for a square lattice in reciprocal space and in the reference frame rotating at the frequency of the coherent pumps can be written as

$$i\dot{a}_{k_x,k_y} = [\omega(k_x, k_y) - \omega_P]a_{k_x,k_y} - i\gamma a_{k_x,k_y} + F_{k_x,k_y}, \qquad (13)$$

where $k_x$ and $k_y$ are the momentum components in the $x$ and $y$ directions, $F_{k_x,k_y} = (1/N)\sum_{n,m} F_{n,m} e^{-i(k_x n + k_y m)}$ is the Fourier transform of the coherent drive, $F_{n,m}$ is the pump amplitude at site $(n, m)$ (where the indices $n, m = -N/2, \ldots, N/2 - 1$ label the lattice sites), and the dispersion relation is given by

$$\omega(k_x, k_y) = \omega_a - 2J[\cos(k_x) + \cos(k_y)], \qquad (14)$$

where $J$ is the tunneling amplitude. In this case, the frequency band extends from $\Delta = -4J$ to $4J$.

By solving for the steady state of the coupled-mode equations, we can calculate the spatial distribution of the intensity inside a $50 \times 50$ lattice. We choose a fixed value of detuning $\Delta = 0$, i.e., at the center of the frequency band. When a single resonant pumping spot is placed at the central site (0,0) (we refer to this configuration as individual driving), light is emitted into the lattice in a collimated fashion, as depicted in Fig. 6(a). This is due to the dispersion relation (14), which leads to a nonuniform group velocity [35,36]. As shown in [23], such collimated emission allows us to find a perfect localization by coupling four pumps at positions $(\pm 1, 0)$ and $(0, \pm 1)$ (we label this configuration collective driving). The resulting spatial intensity distribution is shown in Fig. 6(b), where one can clearly observe the localization of light in the central spot.

This behavior is in agreement with the results of [23]. We now extend them by studying in detail the properties of the total intensity $I_T$ as well as the localization parameter $\lambda$ as the detuning $\Delta$ is varied across the lattice spectrum. Both $I_T$ and $\lambda$ feature a very different behavior in the individual and collective driving configurations. In the former case, the total intensity [see Fig. 6(c)] exhibits a maximum at $\Delta = 0$, i.e., when $\omega_P = \omega_a$, due to the saddle-point region appearing at the center of the dispersion relation. This leads to a vanishing group velocity in a single direction, which is associated with a diverging density of states [44]. As we learned from the 1D case, this implies a peak in $I_T$ at the corresponding value

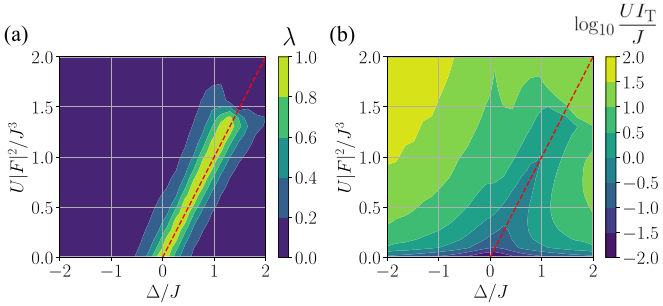


FIG. 7. Localization in the nonlinear square lattice. (a) Localization parameter λ as a function of the pump amplitude $|F|^2$ (normalized in units of the Kerr nonlinearity strength $U$ and the tunneling rate $J$) and the detuning Δ. The red dashed line represents the linear dependence $\Delta = U|F|^2/J^2$. (b) Analogous plot for the total intensity inside the lattice $I_T$. The simulation parameters are the cavity decay rate $\gamma = 5 \times 10^{-2} J$ and $N = 50$, i.e., $50 \times 50$ sites, with open boundary conditions.

of Δ. Regarding the localization parameter λ [see Fig. 6(d)], it is negligible throughout the whole spectrum, except at its edges, i.e., at $\Delta = \pm 4J$, where a small increase is appreciated, corresponding to the vanishing $I_T$. On the other hand, in the collective driving configuration the destructive interference leads to a small (although finite) value of $I_T$ around $\Delta = 0$, irrespective of the vanishing group velocity at that value of detuning [see Fig. 6(e)]. As in the 1D lattice, associated with the minimum of $I_T$, in Fig. 6(f) a maximum of localization in which $\lambda \simeq 1$ appears at $\Delta = 0$.

Overall, we can conclude that in the square lattice there exists an analogous trade-off between localization and total intensity to the one that we already found for the 1D lattice. This hints at a similar behavior when nonlinearities are included in the 2D case. This is what we test in Fig. 7, where we show contour plots of the localization parameter λ [Fig. 7(a)] as well as the total intensity $I_T$ [Fig. 7(b)] as a function of the adimensional parameters $\Delta/J$ and $U|F|^2/J^3$. On the one hand, a finite Kerr nonlinearity enables localization for a range of detunings $\Delta/J \in (0, 1.35)J$, far beyond what can be found in the linear regime, in which localization is restricted to $\Delta = 0$. Above the upper limit of the nonlinear case, located at $\Delta \simeq 1.35J$, dynamical instability suppresses localization, which experiences a sudden drop. As for a 1D lattice with interpump distance $d = 2$, the region of maximum λ follows a linear dependence $\Delta = U|F|^2/J^2$, indicated by the red dashed line in Fig. 7(a). In terms of intensity, Fig. 7(b) shows that a nonzero localization is accompanied by a decreasing $I_T$. To show this, we have also plotted the $\Delta = U|F|^2/J^2$ dependence followed by the region with high localization in Fig. 7(b), showing that the area in which $I_T$ is minimum adheres to the same behavior.

We finish this section by noting that the same conclusions we obtained for the 1D lattice also hold for this 2D lattice: A finite nonlinearity stabilizes localization for a larger range of frequencies than in the absence of nonlinearities. In addition, a large localization is associated with a vanishing intensity inside the lattice, which prevents the exploitation of this phenomenon for the enhancement of nonlinear effects.

## VI. CONCLUSIONS AND OUTLOOK

Summing up, we have studied the phenomenon of driven-dissipative localization in one- and two-dimensional lattices in the presence of optical nonlinearities. We found that the nonlinearity allows us to obtain localization at frequencies different from those observed in the linear regime. In addition, contrary to our initial intuition, such localization does not enhance nonlinear effects due to the concomitant decrease of global intensity inside the lattice. In fact, nonlinear effects such as optical bistabilities occur in regions where the emission between the pumping spots interferes constructively, maximizing the total intensity. We foresee that our results will pave new ways of harnessing nonlinear effects in driven-dissipative systems, e.g., as reconfigurable optical simulator [45–47]. Another direction is to consider the interplay of such driven-dissipative nonlinear effects with topologically nontrivial band structures [16].

*Note added.* Recently, we became aware of Ref. [48], which features some overlapping results for the 1D photonic lattice.

## ACKNOWLEDGMENTS

The authors acknowledge support from the Proyecto Sinérgico CAM 2020 Y2020/TCS-6545 (NanoQuCo-CM), the CSIC Research Platform on Quantum Technologies PTI-001 and from Spanish Projects No. PID2021-127968NB-I00 and No. TED2021-130552B-C22 funded by MCIN/AEI/10.13039/501100011033/FEDER, UE and MCIN/AEI/10.13039/501100011033, respectively. A.M.H. acknowledges support from Fundación General CSIC's ComFuturo program, which has received funding from the European Union's Horizon 2020 research and innovation program under the Marie Skłodowska-Curie Grant Agreement No. 101034263. A.A. acknowledges support from European Research Council grant EmergenTopo (Grant No. 865151), the French government through the Programme Investissement d'Avenir (Grant No. I-SITE ULNE/ANR-16-IDEX-0004 ULNE) managed by the Agence Nationale de la Recherche, the Labex CEMPI (Grant No. ANR-11-LABX-0007), and the region Hauts-de-France. A.G.T. also acknowledges support from a Leonardo Grant for Researchers and Cultural Creators, and from BBVA Foundation. The authors thank Carlos Navarrete-Benlloch for discussion on the solution of non-linear coupled-mode equations.

## APPENDIX A: PHYSICAL IMPLEMENTATION

In this Appendix we assess the experimental realization of our proposal. In particular, we focus on a realistic implementation employing lattices of semiconductor micropillars hosting exciton polaritons [13]. A previous experimental work [22] demonstrated driven-dissipative localization in the linear regime, employing a honeycomb array of micropillars (separated by a distance of 2.3 μm) pumped by a 1.5-eV laser (370 THz, i.e., in the near infrared), with a tunneling rate of 328 μeV (i.e., 79.3 GHz) between nearest-neighbor sites. A polariton lifetime of $\tau = 9$ ps (i.e., $\gamma = 70$ μeV) is small enough to allow one to observe localization with an inverse participation ratio (IPR) of around 0.35 (due to an

unintentional horizontal tilt of the incident laser beams; simulations considering a perfect setup show that it could reach an IPR equal to 0.9).

The crucial question regarding the experimental observation of the nonlinear localization revealed in our work is the inclusion of Kerr nonlinearities. In the case of semiconductor micropillar arrays, the eigenmodes are mixed light-matter quasiparticles called exciton polaritons. They arise from the strong coupling between the photons trapped in the micropillar resonator and the electronic excitations of a semiconductor quantum well embedded in the center of the micropillar. The electronic excitations are known as excitons and they provide repulsive interactions between the polaritons. At the microscopic level, the excitons are composite particles formed by bound electrons and holes. However, when considering polariton-polariton interactions, the complex Coulomb interaction between electrons and holes can be replaced by an effective two-body interaction involving polaritons as a whole [13]. A mean-field approximation allows one to effectively describe the interactions between polaritons with a Kerr-type nonlinearity such as the one employed in our work. The strength of the polariton-polariton interaction can then be regulated by the particle density, which is precisely adjusted by varying the incident laser power.

The polariton interaction needs to be strong enough to allow the adimensional parameter $U|F|^2/J^3$ to show the blueshift of the localization frequencies. Previous works have estimated the polariton interaction strength $U$ to be about 10 μeV μm$^2$ [49,50]. Taking the laser energy to be 1.5 eV in a pumping spot 2.3 μm in diameter (as in Ref. [22]), we get $|F| = 0.67$ eV/μm. Assuming $J = 328$ μeV, one gets an $U|F|^2/J^3$ of the order of $10^5$, much larger than necessary to observe the displacement of the localization frequencies [see Figs. 2(a), 2(c), and 7(a), where $U|F|^2/J^3$ reaches maximum values around 1]. Therefore, we expect our findings to be reproducible with state-of-the-art exciton-polariton experiments.

An alternative implementation can make use of arrays of coupled superconducting resonators working in the microwave regime, where the Kerr nonlinearity is naturally created by the nonlinear inductance of a Josephson junction [51–53].

## APPENDIX B: ANALYTIC EXPRESSIONS FOR THE INTENSITY INSIDE THE 1D LATTICE IN THE LINEAR REGIME

In this Appendix we derive analytical expressions for the spatial distribution of the intensity $|a_n|^2$ as well as for the total intensity $I_T$ in the 1D lattice with nearest-neighbor tunnelings explored in the main text. We first consider the case with two coherent pumps (which can lead to localization) and then for completeness we study a configuration featuring a single pump (in which localization cannot be observed). In all cases, we restrict ourselves to the linear regime, i.e., we set $U = 0$, and consider a lattice formed by $N$ sites.

### 1. Two pumps

Here we assume that the lattice is coherently driven at two sites $n_1$ and $n_2 > n_1$, separated by a distance $d = n_2 - n_1$.

#### *a. Spatial distribution of the intensity*

We now derive an analytical expression for the spatial distribution of the intensity $|a_n|^2$. We start from the coupled-mode equations in reciprocal space for the electric-field amplitudes

$$i\dot{a}_k = -(\Delta + 2J\cos k)a_k - i\gamma a_k + F_k, \tag{B1}$$

where $k$ is the lattice momentum, $a_k = (1/\sqrt{N})\sum_n a_n e^{-ikn}$ and $F_k = (1/\sqrt{N})\sum_n F_n e^{-ikn}$ are the Fourier transforms of the field amplitude and the driving, respectively, $\Delta$ is the laser-resonator detuning, $J$ is the tunneling amplitude between neighboring sites, and $\gamma$ is the cavity decay rate. In the steady state we have that $\dot{a}_k = 0$ and therefore

$$a_k = \frac{F_k}{\Delta + 2J\cos k + i\gamma} \tag{B2}$$

is the steady-state solution of Eq. (B1). Now we explicitly write the expression of $F_k$ for two pumps located at $n_1$ and $n_2$, which takes the shape $F_k = (Fe^{-ikn_1}/\sqrt{N})(1 + e^{-ikd})$. Substituting this into Eq. (B2), transforming to real space, and approximating the discrete sum in momenta by an integral, we get

$$a_n = \frac{1}{\sqrt{N}}\sum_k a_k e^{ikn} \simeq \frac{F}{2\pi}\int_{-\pi}^{+\pi} dk \frac{e^{ik|n-n_1|} + e^{-ik|n-n_2|}}{\Delta + 2J\cos k + i\gamma}. \tag{B3}$$

Here we have assumed that $n$ belongs in the region between the pumps, i.e., $n_1 < n < n_2$. Although the following steps of the derivation correspond to this case, analogous calculations can be carried out for values of $n$ outside that region. The expressions for the two other situations $n < n_1$ and $n > n_2$ are provided in Eq. (9).

We continue the derivation by expanding the denominator of Eq. (B3) around the resonant momenta $k_0 = \pm\arccos(-\Delta/2J)$ up to first order in $k$, obtaining

$$a_n = \frac{F}{2\pi}\int_{-\pi}^{+\pi} dk \Bigg( \frac{e^{ik|n-n_1|} + e^{-ik|n-n_2|}}{-\sqrt{4J^2 - \Delta^2}(k - k_0) + i\gamma} + \frac{e^{ik|n-n_1|} + e^{-ik|n-n_2|}}{\sqrt{4J^2 - \Delta^2}(k + k_0) + i\gamma} \Bigg). \tag{B4}$$

Since the integrands above vanish outside the first Brillouin zone, i.e., from $-\pi$ to $+\pi$, the above integration limits can be extended from $-\infty$ to $+\infty$. Using the residue theorem of complex analysis, we finally obtain

$$a_n = -i\pi F D(\Delta)\big(e^{ik_0|n-n_1|}e^{-\pi\gamma D(\Delta)|n-n_1|} + e^{ik_0|n-n_2|}e^{-\pi\gamma D(\Delta)|n-n_2|}\big), \tag{B5}$$

where $D(\Delta) = 1/\pi\sqrt{4J^2 - \Delta^2}$ is the density of states. The spatial distribution of the intensity $|a_n|^2$ is now obtained by simply taking the square modulus of Eq. (B5). The resulting expression is

$$|a_n|^2 = 2\pi^2|F|^2 D(\Delta)^2 e^{-\pi\gamma D(\Delta)d} \times \{\cosh[\pi\gamma D(\Delta)(n_1 + n_2 - 2n)] + \cos[k_0(n_1 + n_2 - 2n)]\}, \tag{B6}$$

which also appears in Eq. (9).

#### *b. Total intensity*

We now derive an analytic expression for the total intensity $I_T = \sum_n |a_n|^2$. Together with Eq. (B6), this will allow us to calculate the localization parameter $\lambda = \sum_{n_1<n<n_2} |a_n|^2/I_T$. We start by noting that the total intensity can be equivalently written as $I_T = \sum_k |a_k|^2$ in reciprocal space. Thus, we have that

$$I_T \simeq \frac{|F|^2}{2\pi}\int_{-\pi}^{+\pi} dk \frac{2+e^{ikd}+e^{-ikd}}{(\Delta+2J\cos k)^2+\gamma^2}, \tag{B7}$$

where we have employed Eq. (B2) to account for the steady state of $a_k$ in the presence of two pumps separated by a distance $d$ and we have already transformed the discrete sum in momenta to an integral. As we did for $|a_n|^2$, we expand the denominator around the resonant momenta $k_0 = \pm\arccos(-\Delta/2J)$ up to first order in $k$ and we extend the integral from $-\infty$ to $+\infty$, obtaining

$$I_T \simeq \frac{|F|^2}{2\pi}\int_{-\infty}^{+\infty} dk \left( \frac{2+e^{ikd}+e^{-ikd}}{(4J^2-\Delta^2)(k+k_0)+\gamma^2} + \frac{2+e^{ikd}+e^{-ikd}}{(4J^2-\Delta^2)(k-k_0)+\gamma^2} \right). \tag{B8}$$

The integral above can be calculated by applying the residue theorem of complex analysis, which finally yields Eq. (10).

### 2. Single pump

Here we consider a single coherent pump driving the site $n_1$ of the linear ($U = 0$) 1D lattice with first-neighbor couplings. Below these lines we provide analytic expressions for the spatial distribution of the intensity $|a_n|^2$ as well as for the total intensity $I_T$. The calculations are analogous to those of Appendix B 1 and therefore we skip some details.

#### *a. Spatial distribution of the intensity*

We start with the derivation of the spatial distribution of the intensity $|a_n|^2$. As in Appendix B 1 a, we use Eq. (B2) to account for the steady state of the coupled-mode equations (B1). However, for a single pump we use $F_k = (1/\sqrt{N})Fe^{-ikn_1}$ as the explicit expression for the coherent drive in Fourier space. In the following, we assume $n > n_1$. In spite of this, a completely analogous calculation can be carried for $n_1 < n$. Overall, we get

$$\begin{aligned} a_n &= \frac{1}{\sqrt{N}}\sum_k a_k e^{ikn} \\ &\simeq -\frac{FD(\Delta)}{2}\int_{-\infty}^{+\infty} dk \left( \frac{e^{ik|n-n_1|}}{k-k_0-i\pi\gamma D(\Delta)} \times -\frac{e^{ik|n-n_1|}}{k+k_0+i\pi\gamma D(\Delta)} \right), \end{aligned} \tag{B9}$$

where we have approximated the discrete sum by an integral whose limits can be extended to $\pm\infty$. We have also expanded the denominator of the steady-state solution $\Delta + 2J\cos k + i\gamma$ around the resonant momenta $k_0 = \pm\arccos(-\Delta/2J)$ up to first order in $k$.

As a final step, we evaluate the integrals above using the residue theorem of complex analysis. This gives

$$a_n = -i\pi F D(\Delta) e^{ik_0|n-n_1|} e^{-\pi\gamma D(\Delta)|n-n_1|}. \tag{B10}$$

The intensity distribution $|a_n|^2$ is simply the square modulus of this equation. By replicating this calculation with $n_1 < n$ we arrive at the expression

$$|a_n|^2 = \begin{cases} \pi^2|F|^2D(\Delta)^2 e^{2\pi\gamma D(\Delta)|n-n_1|} & \text{if } n \leqslant n_1 \\ \pi^2|F|^2D(\Delta)^2 e^{-2\pi\gamma D(\Delta)|n-n_1|} & \text{if } n \geqslant n_1. \end{cases} \tag{B11}$$

#### *b. Total intensity*

Finally, the total intensity $I_T$ when a single pump is coherently driving the site $n_1$ of the lattice is given by

$$\begin{aligned} I_T = \sum_k |a_k|^2 &\simeq \frac{|F|^2}{2\pi}\int_{-\pi}^{+\pi} dk \frac{1}{(\Delta+2J\cos k)^2+\gamma^2} \\ &\simeq \frac{|F|^2}{2\pi}\int_{-\infty}^{+\infty} dk \left( \frac{1}{(4J^2-\Delta^2)(k+k_0)^2+[\pi\gamma D(\Delta)]^2} + \frac{1}{(4J^2-\Delta^2)(k-k_0)^2+[\pi\gamma D(\Delta)]^2} \right), \end{aligned} \tag{B12}$$

where we have employed the same approximations as in Appendix B 2 a. After computing the integrals by means of the residue theorem of complex analysis, the equation above yields

$$I_T = \frac{\pi|F|^2 D(\Delta)}{\gamma}. \tag{B13}$$

## APPENDIX C: ANALOGY BETWEEN MULTIPLE DRIVINGS AND SPONTANEOUS EMISSION OF MULTIPLE EMITTERS

Following the path opened by Ref. [23], in this Appendix we provide more details on the analogy between probing the properties of lossy photonic lattices by coherently driving them and by means of quantum emitters. In particular, we note that the total intensity $I_T$ inside a driven-dissipative lattice is proportional to the local density of states (LDOS) when the pumps are replaced by quantum emitters at the same spots. The LDOS measures the number of electromagnetic modes available at a given point in space and therefore contains information about how the radiative properties of the emitter are modified by its coupling to a structured bath [35–37].

Below we calculate the LDOS for the 1D and 2D lattices studied in the main text. We consider quantum emitters coupled to the same spots in which coherent drives would be able to produce localization. In the two cases, we restrict ourselves to the linear regime, i.e., $U = 0$.

### 1. 1D lattice

Here we consider a 1D photonic lattice formed by $N$ sites with first-neighbor couplings. This is coupled to two quantum emitters at sites $n_1$ and $n_2$, separated by a distance $d = n_2 - n_1$. To calculate the LDOS we first need to compute the self-energy of the quantum emitter $\Sigma_e(\Delta + i\gamma)$ for an emitter-resonator detuning $\Delta$ and a photonic cavity decay rate $\gamma$. Such a quantity captures the effect of the coupling to the

lattice on the quantum emitter. If we assume an emitter-photon coupling of strength $g$, the self-energy reads

$$\Sigma_e(\Delta + i\gamma) = \frac{1}{N}\sum_k \frac{|ge^{-ikn_1} + ge^{-ikn_2}|^2}{\Delta + 2J\cos k + i\gamma}. \quad \text{(C1)}$$

The LDOS is then given by twice its imaginary part, i.e.,

$$\Gamma_e = -2\,\mathrm{Im}[\Sigma_e(\Delta + i\gamma)]$$
$$\simeq \frac{|g|^2\gamma}{2\pi}\int_{-\pi}^{+\pi} dk \frac{2 + e^{ikd} + e^{-ikd}}{(\Delta + 2J\cos k)^2 + \gamma^2}. \quad \text{(C2)}$$

This integral is the same as the one calculated in Eq. (B7) to compute the total intensity of a 1D lattice driven by two pumps. Therefore, we get

$$\Gamma_e(\Delta) = 4\pi|g|^2 D(\Delta)[1 + \cos(k_0 d)e^{-\pi\gamma D(\Delta)d}]. \quad \text{(C3)}$$

The above expression follows the same functional dependence of Eq. (10) but makes the substitution $g \leftrightarrow F/\sqrt{2\gamma}$.

Therefore, the light-matter coupling in the quantum emitter picture plays the role of the coherent pump amplitudes in the driven-dissipative setup. Although this was already demonstrated by Ref. [23], in this Appendix we revealed the connection between the total intensity and the LDOS. Such a connection can be employed to measure the LDOS by means of the total intensity, which is more experimentally accessible. In addition, the correspondence between these two quantities allows us to regard the vanishing total intensity which accompanies a high localization parameter as an inefficient coupling of the coherent drivings to the photonic lattice.

### 2. 2D lattice

We now consider a 2D square lattice with $N \times N$ sites and first-neighbor couplings. Four quantum emitters are coupled sites $(\pm 1, 0)$ and $(0, \pm 1)$, where the intersite distance is 1 and (0,0) is the central site. The self-energy of the quantum emitters reads

$$\Sigma_e(\Delta + i\gamma) = \frac{1}{N^2}\sum_{k_x,k_y} \frac{|ge^{-ik_x d} + ge^{ik_x d} + ge^{-ik_y d} + ge^{ik_y d}|^2}{\Delta + 2J(\cos k_x + \cos k_y) + i\gamma}. \quad \text{(C4)}$$

Although it is difficult to analytically perform the calculation above, even by transforming the sum into an integral, we can still calculate the self-energy numerically. As in the 1D case, the LDOS is then evaluated as $\Gamma_e = -2\,\mathrm{Im}[\Sigma_e(\Delta + i\gamma)]$.

The resulting LDOS is shown in Fig. 8, where we compare it with the total intensity $I_T$ of a driven-dissipative square lattice with four coherent pumps located at the same positions as the emitters, as was studied in Sec. V. The total intensity is rescaled using a proportionality factor $\alpha \simeq 0.11$ in order to show that, as in the 1D case, the LDOS of the square lattice is proportional to $I_T$.

Finally, Fig. 8 also compares the LDOS of the square lattice with the one of the 1D lattice [given by Eq. (C3)]. As we can see, the main difference between them is that the LDOS of the 1D lattice diverges at its band edges ($\Delta = \pm 2J$), while that of the square lattice reaches a constant value at the corresponding band edges ($\Delta = \pm 4J$). We note that this provides some intuition behind the fact that the dynamical instability

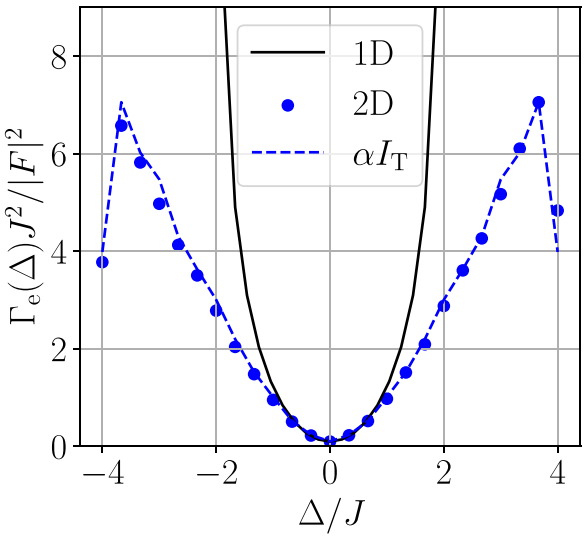


FIG. 8. The black solid line shows the LDOS $\Gamma_e$ (normalized in units of the tunneling rate $J$ and the pump intensity $|F|^2$) for two quantum emitters coupled at two different sites separated by a distance $d = 2$ in a 1D lattice. Blue circles show the LDOS for four quantum emitters coupled to sites $(\pm 1, 0)$ and $(0, \pm 1)$ of a 2D square lattice. Both LDOSs are plotted as a function of the detuning $\Delta$. The blue dashed line shows the total intensity $I_T$ in the driven-dissipative 2D lattice [under coherent pumping at sites $(\pm 1, 0)$ and $(0, \pm 1)$] multiplied by a proportionality factor $\alpha \simeq 0.11$. The simulation parameters are the cavity decay rate $\gamma = 5 \times 10^{-2} J$ and the number of sites $100 \times 100$ to calculate the LDOS of the square lattice and $50 \times 50$ to compute its $I_T$.

observed in the calculations shown in Figs. 3 and 7 appears for a smaller value of detuning in the 1D lattice compared to the 2D one. As a larger number of states (given by the diverging LDOS) is available in the former situation, parametric terms coupling different momenta are more important and thus drive the dynamical instability sooner than when the 2D lattice is considered. More information on the role of parametric terms is provided in Appendix D.

## APPENDIX D: DYNAMICAL INSTABILITY IN MOMENTUM SPACE

In this Appendix we perform a Bogoliubov analysis of the dynamical stability in the 1D lattice. Our intuition is that the parametric terms coupling different momenta give rise to dynamical instability for large values of detuning $\Delta$ and pump intensity $|F|^2$, thus destroying localization. We consider a driving configuration with two pumps separated by a distance $d = 2$.

We begin by transforming the nonlinear coupled-mode equations (1) into reciprocal space

$$i\dot{a}_k = -(\Delta + 2J\cos k)a_k + \frac{U}{N}\sum_{q,q'} a^*_{q+q'-k}a_q a_{q'} - i\gamma a_k + F_k, \quad \text{(D1)}$$

where $a_k = (1/\sqrt{N})\sum_n a_n e^{-ikn}$ and $F_k = (1/\sqrt{N})\sum_n F_n e^{-ikn}$ are the Fourier transforms of the electric-field amplitude and the coherent driving, respectively, and the lattice momentum

$k$ runs from $-\pi$ to $\pi$ with steps $2\pi/N$. Parametric terms appear due to the Kerr nonlinearity and they couple different momenta while satisfying the conservation law for such a quantity.

In principle, we need to take into account all terms appearing in the double sum of Eq. (D1). However, to study the appearance of instability in more detail we start by considering independently all the different coupling terms in $k$. Although these approximations are by no means justified (a localized intensity in real space results in the population of all momenta in reciprocal space), we use them as a first step to understand better the role of the different parametric terms.

We start by considering the self-Kerr interaction, which results in the coupled-mode equations

$$i\dot{a}_k = -(\Delta + 2J\cos k)a_k + \frac{U}{N}|a_k|^2 a_k - i\gamma a_k + F_k. \quad \text{(D2)}$$

In order to study the stability of small fluctuations around the steady state, we make the substitution $a_k \to a_k^{(\mathrm{ss})} + \delta a_k$ in Eq. (D2), where $a_k^{(\mathrm{ss})}$ is the steady state reached at $t \to \infty$ and $\delta a_k$ are the small fluctuations around it. We then linearize the resulting equations with respect to $\delta a_k$, obtaining the Bogoliubov coupled-mode equations for the small fluctuations

$$i\delta\dot{a}_k = -(\Delta + 2J\cos k)\delta a_k + 2U\left|a_k^{(\mathrm{ss})}\right|^2\delta a_k + U{a_k^{(\mathrm{ss})}}^2\delta a_k^* - i\gamma\delta a_k, \quad \text{(D3)}$$

$$i\delta\dot{a}_k^* = (\Delta + 2J\cos k)\delta a_k - 2U\left|a_k^{(\mathrm{ss})}\right|^2\delta a_k^* - U{a_k^{(\mathrm{ss})}}^2\delta a_k - i\gamma\delta a_k. \quad \text{(D4)}$$

Using the vector form $\boldsymbol{\delta a} = [\delta a_{-\pi}, \ldots, \delta a_{\pi}]^{\mathrm{T}}$, we can write the linear system of equations above in the more compact form

$$i\frac{d}{dt}\boldsymbol{\delta a} = A\boldsymbol{\delta a}. \quad \text{(D5)}$$

To assess the dynamical stability of the steady state against small fluctuations, we can diagonalize the matrix $A$ and look at the sign of the imaginary part of its eigenvalues $\mathrm{Im}(w)$. Dynamical instability arises whenever there is at least one eigenvalue featuring a positive imaginary part [13,54].

Figure 9(a) plots $\mathrm{Im}(w)$ as a function of $\Delta$ across the path $\Delta = U|F|^2/J^2$ where localization appears. For comparison, we also show $\mathrm{Im}(w)$ in the linear regime (i.e., by setting $U = 0$) as a yellow dashed line. As expected, in the linear case $\mathrm{Im}(w) = -\gamma$ regardless of $\Delta$, meaning that the system can never become dynamically unstable. However, when a finite value of $U$ is added, the self-Kerr interaction makes the imaginary part of some eigenvalues depart from their linear values, effectively broadening $\mathrm{Im}(w)$. This takes place near the upper band edge, located at $\Delta = 2J$, which agrees with the fact that dynamical instability is observed for growing $\Delta$ when all terms in Eq. (D1) are taken into account. However, as we see from Fig. 9(a), dynamical instability cannot be induced by self-Kerr terms alone.

The next order in our expansion is parametric terms coupling neighboring momenta, i.e., each value of $k$ with its corresponding $k \pm 2\pi/N$. The coupled-mode equations read,

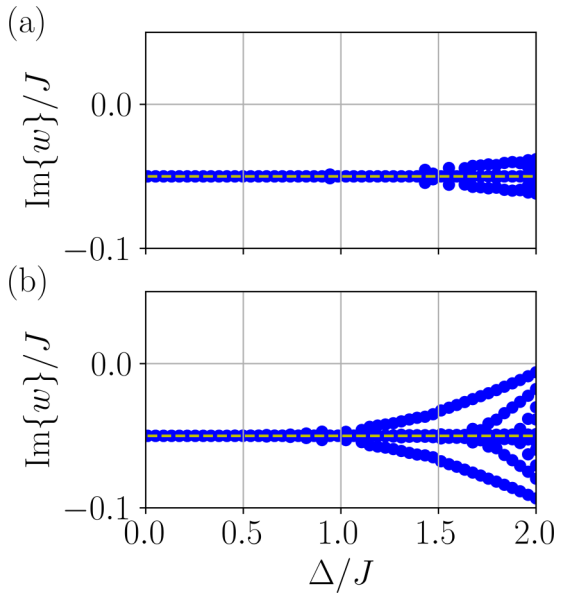


FIG. 9. Dynamical stability in the 1D lattice coherently driven by two pumps separated by a distance $d = 2$. The imaginary part of the eigenvalues $\mathrm{Im}(w)$ of the Bogoliubov matrix $A$ (see the text for details) is plotted as a function of the detuning $\Delta$ (both quantities are normalized in units of the tunneling rate $J$) along the $\Delta = U|F|^2/J^2$ path, where $U$ is the Kerr nonlinearity strength and $|F|^2$ is the pump intensity for (a) self-Kerr interaction and (b) first-neighbor Kerr interaction. In both plots the yellow dashed line represents the linear solution $\mathrm{Im}(w) = -\gamma$. The simulation parameters are the cavity decay rate $\gamma = 5 \times 10^{-2}$, $N = 500$ sites with open boundary conditions, and $n_1 = 250$.

in that case,

$$i\dot{a}_k = -(\Delta + 2J\cos k)a_k + \frac{U}{N}|a_k|^2 a_k + 2\frac{U}{N}|a_{k+2\pi/N}|^2 a_k + 2\frac{U}{N}|a_{k-2\pi/N}|^2 a_k + 2\frac{U}{N}a_k^* a_{k+2\pi/N} a_{k-2\pi/N} - i\gamma a_k + F_k. \quad \text{(D6)}$$

An analogous Bogoliubov analysis can be performed in this case as well. The imaginary part of the eigenvalues of the matrix $A$ governing the dynamics of linearized fluctuations is shown in Fig. 9(b) as a function of $\Delta$ across the $\Delta = U|F|^2/J^2$ path. Even though the system is still dynamically stable along the whole path, some imaginary parts depart from the linear solution $\mathrm{Im}(w) = -\gamma$ sooner than when only self-Kerr terms are present, and they even reach $\mathrm{Im}(w) = 0$ at the upper band edge, i.e., at $\Delta = 2J$.

In conclusion, parametric couplings between different values of $k$ result in some $\mathrm{Im}(w)$ departing from their linear value and approaching zero. Our intuition is that the inclusion of the rest of the parametric terms in Eq. (D1) results in the appearance of a dynamical instability near the upper band edge, which is what we observe when we solve the coupled-mode equations in real space (1), as it is shown in Figs. 3 and 7.

[1] P. W. Anderson, Phys. Rev. **109**, 1492 (1958).
[2] P. A. Lee and T. V. Ramakrishnan, Rev. Mod. Phys. **57**, 287 (1985).
[3] T. R. Kirkpatrick, Phys. Rev. B **31**, 5746 (1985).
[4] H. Hu, A. Strybulevych, J. H. Page, S. E. Skipetrov, and B. A. van Tiggelen, Nat. Phys. **4**, 945 (2008).
[5] T. Schwartz, G. Bartal, S. Fishman, and M. Segev, Nature (London) **446**, 52 (2007).
[6] L. Levi, M. Rechtsman, B. Freedman, T. Schwartz, O. Manela, and M. Segev, Science **332**, 1541 (2011).
[7] V. Goblot, A. Štrkalj, N. Pernet, J. L. Lado, C. Dorow, A. Lemaître, L. Le Gratiet, A. Harouri, I. Sagnes, S. Ravets, A. Amo, J. Bloch, and O. Zilberberg, Nat. Phys. **16**, 832 (2020).
[8] S. Haroche, Rev. Mod. Phys. **85**, 1083 (2013).
[9] H. J. Kimble, Nature (London) **453**, 1023 (2008).
[10] A. Reiserer and G. Rempe, Rev. Mod. Phys. **87**, 1379 (2015).
[11] A. Reiserer, Rev. Mod. Phys. **94**, 041003 (2022).
[12] H. Ritsch, P. Domokos, F. Brennecke, and T. Esslinger, Rev. Mod. Phys. **85**, 553 (2013).
[13] I. Carusotto and C. Ciuti, Rev. Mod. Phys. **85**, 299 (2013).
[14] J. D. Joannopoulos, P. R. Villeneuve, and S. Fan, Nature (London) **386**, 143 (1997).
[15] T. W. Ebbesen, C. Genet, and S. I. Bozhevolnyi, Phys. Today **61** (5), 44 (2008).
[16] T. Ozawa, H. M. Price, A. Amo, N. Goldman, M. Hafezi, L. Lu, M. C. Rechtsman, D. Schuster, J. Simon, O. Zilberberg, and I. Carusotto, Rev. Mod. Phys. **91**, 015006 (2019).
[17] P. St-Jean, V. Goblot, E. Galopin, A. Lemaître, T. Ozawa, L. Le Gratiet, I. Sagnes, J. Bloch, and A. Amo, Nat. Photon. **11**, 651 (2017).
[18] J. von Neumann and E. P. Wigner, in *The Collected Works of Eugene Paul Wigner*, edited by A. S. Wightman (Springer, Berlin, 1993), Vol. A, pp. 291–293.
[19] C. W. Hsu, B. Zhen, A. D. Stone, J. D. Joannopoulos, and M. Soljačić, Nat. Rev. Mater. **1**, 16048 (2016).
[20] S. Sugimoto, Y. Ashida, and M. Ueda, arXiv:2307.05456.
[21] B. Huang, Y. Ke, H. Zhong, Y. S. Kivshar, and C. Lee, arXiv:2312.15664.
[22] O. Jamadi, O. Jamadi, B. Real, K. Sawicki, C. Hainaut, A. González-Tudela, N. Pernet, I. Sagnes, M. Morassi, A. Lemaître, L. L. Gratiet, A. Harouri, S. Ravets, J. Bloch, and A. Amo, Optica **9**, 706 (2022).
[23] A. Gonzalez-Tudela, New J. Phys. **24**, 043001 (2022).
[24] P. N. Butcher and D. Cotter, *The Elements of Nonlinear Optics* (Cambridge University Press, Cambridge, 2008).
[25] A. Dousse, J. Suffczyński, A. Beveratos, O. Krebs, A. Lemaître, I. Sagnes, J. Bloch, P. Voisin, and P. Senellart, Nature (London) **466**, 217 (2010).
[26] T. Jacqmin, I. Carusotto, I. Sagnes, M. Abbarchi, D. D. Solnyshkov, G. Malpuech, E. Galopin, A. Lemaître, J. Bloch, and A. Amo, Phys. Rev. Lett. **112**, 116402 (2014).
[27] A. Blais, S. M. Girvin, and W. D. Oliver, Nat. Phys. **16**, 247 (2020).
[28] I. Carusotto, A. A. Houck, A. J. Kollár, P. Roushan, D. I. Schuster, and J. Simon, Nat. Phys. **16**, 268 (2020).
[29] A. Blais, A. L. Grimsmo, S. M. Girvin, and A. Wallraff, Rev. Mod. Phys. **93**, 025005 (2021).
[30] J. C. Owens, M. G. Panetta, B. Saxberg, G. Roberts, S. Chakram, R. Ma, A. Vrajitoarea, J. Simon, and D. I. Schuster, Nat. Phys. **18**, 1048 (2022).
[31] S. Fan, W. Suh, and J. D. Joannopoulos, J. Opt. Soc. Am. A **20**, 569 (2003).
[32] D. Walls and G. Milburn, *Quantum Optics* (Springer, Berlin, 2008).
[33] Codes to reproduce the results of this paper are available at https://github.com/albertomdlh/non-linear-localization.
[34] R. Román-Ancheyta, B. Çakmak, R. J. León-Montiel, and A. Perez-Leija, Phys. Rev. A **103**, 033520 (2021).
[35] A. González-Tudela and J. I. Cirac, Phys. Rev. Lett. **119**, 143602 (2017).
[36] A. González-Tudela and J. I. Cirac, Phys. Rev. A **96**, 043811 (2017).
[37] W. L. Barnes, S. A. R. Horsley, and W. L. Vos, J. Opt. **22**, 073501 (2020).
[38] T. Baba, Nat. Photon. **2**, 465 (2008).
[39] G. Calajó, F. Ciccarello, D. Chang, and P. Rabl, Phys. Rev. A **93**, 033833 (2016).
[40] P. K. Shukla and J. J. Rasmussen, Opt. Lett. **11**, 171 (1986).
[41] M. Nakazawa, K. Suzuki, and H. A. Haus, Phys. Rev. A **38**, 5193 (1988).
[42] S. Trillo and S. Wabnitz, Opt. Lett. **16**, 986 (1991).
[43] I. Carusotto and C. Ciuti, Phys. Rev. Lett. **93**, 166401 (2004).
[44] N. W. Ashcroft and N. D. Mermin, *Solid State Physics* (Harcourt, Fort Worth, 1976), p. 95.
[45] N. G. Berloff, M. Silva, K. Kalinin, A. Askitopoulos, J. D. Töpfer, P. Cilibrizzi, W. Langbein, and P. G. Lagoudakis, Nat. Mater. **16**, 1120 (2017).
[46] K. P. Kalinin and N. G. Berloff, Phys. Rev. Lett. **121**, 235302 (2018).
[47] K. P. Kalinin and N. G. Berloff, Phys. Rev. B **100**, 245306 (2019).
[48] G. Usaj, arXiv:2402.09104.
[49] A. Amo, J. Lefrère, S. Pigeon, C. Adrados, C. Ciuti, I. Carusotto, R. Houdré, E. Giacobino, and A. Bramati, Nat. Phys. **5**, 805 (2009).
[50] Y. Sun, Y. Yoon, M. Steger, G. Liu, L. N. Pfeiffer, K. West, D. W. Snoke, and K. A. Nelson, Nat. Phys. **13**, 870 (2017).
[51] J. Koch, T. M. Yu, J. Gambetta, A. A. Houck, D. I. Schuster, J. Majer, A. Blais, M. H. Devoret, S. M. Girvin, and R. J. Schoelkopf, Phys. Rev. A **76**, 042319 (2007).
[52] G. Kirchmair, B. Vlastakis, Z. Leghtas, S. E. Nigg, H. Paik, E. Ginossar, M. Mirrahimi, L. Frunzio, S. M. Girvin, and R. J. Schoelkopf, Nature (London) **495**, 205 (2013).
[53] S. Puri, C. K. Andersen, A. L. Grimsmo, and A. Blais, Nat. Commun. **8**, 15785 (2017).
[54] A. M. de las Heras and I. Carusotto, Phys. Rev. A **104**, 043501 (2021).